Status of the MQXFB Nb_3Sn quadrupoles for the HL-LHC

Susana Izquierdo Bermudez, Giorgio Ambrosio, Giorgio Apollinari, Amalia Ballarino, Christian Barth, Mickael Denis Crouvizier, Delio Duarte Ramos, Arnaud Devred, Sandor Feher, Helene Felice, Paolo Ferracin, Jose Ferradas Troitino, Michael Guinchard, Nicholas Lusa, Franco Mangiarotti, Attilio Milanese, Alice Moros, Herve Prin, Stephan Russenschuck, Stefano Sgobba, Ezio Todesco, Gerard Willering.

***Abstract* - The cold powering test of the first two prototypes of the MQXFB quadrupoles (MQXFBP1, now disassembled, and MQXFBP2), the Nb_3Sn inner triplet magnets to be installed in the HL-LHC, has validated many features of the design, such as field quality and quench protection, but has found performance limitations. In fact, both magnets showed a similar phenomenology, characterized by reproducible quenches in the straight part inner layer pole turn, with absence of training and limiting the performance at 93% (MQXFBP1) and 98% (MQXFBP2) of the nominal current at 1.9 K, required for HL-LHC operation at 7 TeV. Microstructural inspections of the quenching section of the limiting coil in MQXFBP1 have identified fractured Nb_3Sn filaments in strands located at one specific position of the inner layer pole turn, allowing to determine the precise origin of the performance limitation. In this paper we outline the strategy that has been defined to address the possible sources of performance limitation, namely coil manufacturing, magnet assembly and integration in the cold mass.**

***Index Terms*—Nb_3Sn, Accelerator Magnets, HL-LHC**

I. Introduction

THE High Luminosity Upgrade of the Large Hadron Collider aims at increasing the integrated luminosity by a factor 10 [1]. One of the main components of the upgrade are the triplet quadrupoles (Q1, Q2a, Q2b, Q3) [2]. With respect to the current triplet quadrupoles, the new magnets called MQXF, will feature a larger aperture, from 70 mm to 150 mm, a higher peak field, from 8.6 T to 11.3 T, and a different superconducting material, Nb_3Sn instead of Nb-Ti [3]. The magnetic length of Q1/Q3 is 8.4 m, split in two magnets of 4.2 m (MQXFA) which are being fabricated by the US Accelerator Research Program (AUP) [4], a continuation of LARP (LHC Accelerator Research [5]). CERN is in charge of MQXFB, the 7.2 m long magnets that will be inserted in a single cold mass for the Q2a and Q2b. MQXFA and MQXFB have identical cross-sections and 3D design. After a series of short models constructed in close collaboration by LARP and CERN [6], the development program at CERN is in the prototyping phase, assembling and testing full-length magnets.

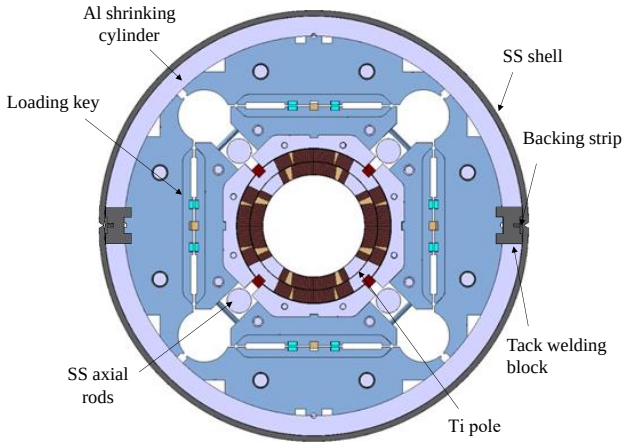

Fig. 1. MQXF magnet cross section

The magnet design relies on a system of water pressurized bladders and keys to apply a pre-stress to coil-pack and to pre-tension the aluminum shrinking cylinder at room temperature [6][7]. After loading, two 8-mm thick stainless-steel (SS) half shells are welded around the magnet to provide a LHe vessel. The cold mass assembly is completed with the welding of the end covers to the main cylinder formed by the welded shells. Due to the impossibility to access the reverse side of the longitudinal weld of the shrinkage cylinders, a permanent backing strip has been chosen, to provide support for a fully penetrated root pass. The backing strip is linked to the magnet through tack welding blocks every 0.6 m that can slide in the direction of the magnet axis to compensate for the different in thermal contraction among the different components. The cross-section of the magnet is shown in Fig. 1.

II. Main Findings

The test of the two first prototype quadrupoles, MQXFBP1 and MQXFBP2, has validated many features of the design such as field quality and quench protection, but has found a

Manuscript receipt and acceptance dates will be inserted here.
(Corresponding author: susana.izquierdo.bermudez@cern.ch*)*
Susana Izquierdo Bermudez, Amalia Ballarino, Christian Barth, Mickael Denis Crouvizier, Arnaud Devred, Delio Duarte Ramos, Helene Felice, Jose Ferradas Troitino, Nicholas Lusa, Franco Mangiarotti, Michael Guinchard, Attilio Milanese, Alice Moros, Herve Prin, Stephan Russenschuck, Stefano Sgobba, Ezio Todesco, Gerard Willering are with CERN, CH-1211 Geneva 23, Switzerland.
Giorgio Ambrosio, Giorgio Apollinari, Sandor Feher are with Fermi National Accelerator Laboratory (FNAL), Batavia, IL 60510 USA.
Paolo Ferracin is with Lawrence Berkeley National Laboratory (LBNL), Berkley, CA 94720 USA.
Color versions of one or more of the figures in this paper are available online at http://ieeexplore.ieee.org.
Digital Object Identifier will be inserted here upon acceptance.

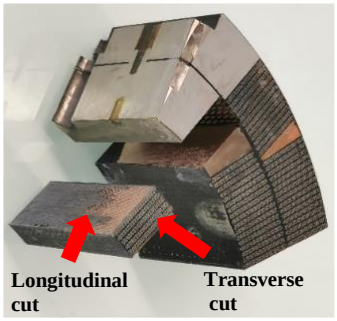

Fig 2. Extracted longitudinal sample indicating the longitudinal and transverse directions for the cut.

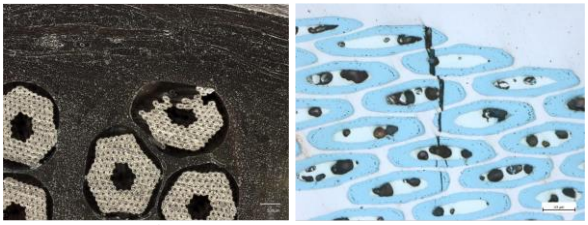

Fig. 3. Example of transversal cracks through optical microscopy examination of a coil transverse cross-section after copper etching (left) and transversal cracks observed along the strands axis by preparing a longitudinal cross-section after fine polishing and grinding (right) [11].

performance limitation with a very similar phenomenology. Both MQXFBP1 (tested in summer 2020) and MQXFBP2 (tested in spring 2021) were limited at 1.9 K at 93 % and 98 % of the nominal current required for HL-LHC operation at 7 TeV (16.23 kA). The first prototype MQXFBP1 has been disassembled and the limiting coil has been inspected via non-destructive and destructive tests. The second prototype, MQXFBP2, after the first test, has been used to validate the trimmed powering scheme in fall 2021 and is being assembled in the first Q2 prototype cold mass, validating all constructions steps, including the integration of the nested corrector and busbars. This section summarizes the main outcomes from the power tests and the findings from the post-mortem inspection of coils.

A. Cold powering test results

Nominal current for operation at 7 TeV is 16.23 kA. MQXFBP1 reached a quench limit during the first ramp with nominal ramp rate at 1.9 K, at 15.17 kA in coil 108 (P3). After one training quench, MQXFBP2, was limited at 15.95 kA at 1.9 K and nominal ramp rate (20 A/s) in coil 113 (P1). At 4.5 K, the quench current was 13.85 kA in MQXFBP1 and 14.45 kA in MQXFBP2, compatible with a magnet on the critical surface (70% of the short sample limit in MQXFBP1, 73 % in MQXFBP2, both at 1.9 K and 4.5 K). Both magnets show early superconducting-normal transition, with decaying voltages as observed on others Nb_3Sn accelerator magnets at CERN [8]. The quench propagation velocity was like other MQXF short magnets at similar level of current, pointing towards local damage of the superconductor. All quenches except those at the highest ramp rate were in the same coil, both at 1.9 K and 4.5 K. In all the cases, the quench starts in the inner layer pole turn. The longitudinal position of the quench initiation was derived from the quench antenna signals, and it was in all the cases close to the magnet mechanical center [9].

In MQXFBP2, to bypass the limitation imposed by the limiting coil and probe the behaviour of the rest of the windings, a novel procedure to inject less current in the limiting coil was developed, referred to as “trim powering”. A 2 kA DC power converter was connected using the CLIQ lead [10] to allow powering the magnet with reduced current in coil 113 (P1). Two out of the other three coils were limited at 500-600 A higher than the limiting coil 113 [9]. At 1.9 K with a ramp of 1 A/s, coils 110, 111 and 112 reached 17 kA without quench. V-I measurements showed a voltage build-up in the quenching segment in coil 113, both at 1.9 and 4.5 K. Some segments in coils 112 and 111 also showed a smaller voltage build-up at 4.5 K.

B. Coil post-mortem examination

Based on the analysis of voltage taps and quench antennas, metallurgical inspection was performed in the limiting coil of MQXFBP1, coil 108, to explore the root-causes of the quenches. The focus here are the full transverse cracks of Nb_3Sn sub-elements (perpendicular to the longitudinal axis of the strands) and causing a degradation in the wire critical current (I_c) [11]. Radial micro cracks were also found, 20-30 µm deep, parallel to the longitudinal axis of the strands; such micro-cracks are not expected to create discontinuity through the current-carrying superconducting phase [12]. The inspection starts with the extraction of the coil volume containing the plane(s) of interest using a diamond wire saw to minimize any artifact coming from the cutting process. The typical length of the samples is 50 mm (see Fig. 2). After a light polishing of the coil-slice, a Cu etching process is carried out in several steps, to remove 0.5 – 0.6 mm of copper. Through the removal of copper, broken filaments are clearly visible when transverse cracks are present (Fig. 3, left). The extension of the damage can be studied through a longitudinal cut, parallel to the direction of the Rutherford cable. After a fine grinding and polishing, optical observation of the samples allows to understand

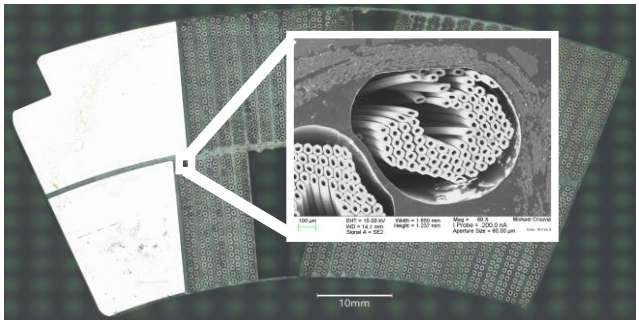

Fig. 4. Collapsed filaments in coil 108 [11].

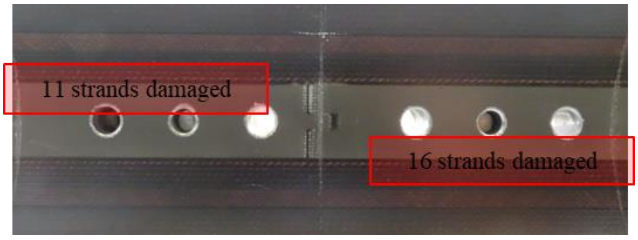

Fig. 5. Extension of the damaged in coil 108 quenching segment.

the extent of the transversal crack-events along the strand axis [11]. Figure 3, right, shows the typical view of a transversal crack observed along the strand axis.

In January 2022, after copper etching, transverse cracks were observed in one strand located at the upper edge of the inner layer pole turn of coil 108, as shown in Fig. 4, with a full breakage of around one fourth of the hundred sub-elements in that specific strand. All the rest of the sub-elements in the entire coil cross section were intact. To further characterize the extension of the damage, longitudinal cuts were performed in the two quenching regions of coil 108. The limiting segment at 4.5 K revealed 16 strands with broken filaments, whereas 11 strands were affected in the limiting segment at 1.9 K. The total damaged length was 90 mm over 160 mm, centered around the transitions of the titanium (Ti) poles in the longitudinal direction (see Fig. 5).

Since the study of longitudinal cuts is very demanding (16 h per 50 mm sample, vs 5 h for a coil cross section analysis through copper etching), it was decided to study 1 m of coil with 50 mm granularity through copper etching. Broken sub-elements were found in strands at the top edge of the inner layer pole turn, close to the Ti pole-to-pole transitions which was a clear indication of a weakness in that area. The poles are around 400 mm long with 20 mm staggering between the inner and outer layer pole, with a total number of transitions per coil of 16. In coil 108, 7 out of the 16 were inspected through copper etching, and broken sub-elements were found in 4 transitions, always in the strand at the top edge of the inner layer pole turn. Two more longitudinal cuts were analyzed, with an extension of the damaged area of 15 mm in a 50 mm length sample and 20 mm in a 30 mm length sample.

III. The Strategy

In Spring 2021, after the test of MQXFBP2, the production was stopped to identify and address possible root causes for the performance limitation. Three possible root causes have been identified for the performance limitation: 1) Cold mass assembly, with a non-optimum mechanical coupling between the welded outer stainless steel and the magnet structure, leading to excessive peak stress in the coils; 2) Magnet assembly, with non-optimum magnet assembly parameters and processes (e.g., keying and bladdering), again, leading to excessive peak stresses on coils; 3) Coil manufacturing, with issues during coil manufacturing and/or handling leading to coil non-uniformities and/or deformation. We cannot exclude that the performance limitation may come from a combination of two of the three, or of all of them. Note that the MQXFA program has demonstrated that coil manufacturing/handling (Cause 3) and magnet assembly (Cause 2) can be successfully developed and applied to coil and magnet assembly up to 4.2 m. Due to manufacturing lead times, the three root causes can only be addressed in "reverse order" (shell welding, then magnet assembly, then coil manufacturing), but the results of each step can be fed into the next one.

To address Cause 1, a revised welding procedure, aimed at minimizing the impact of the stainless-steel shell on the strain

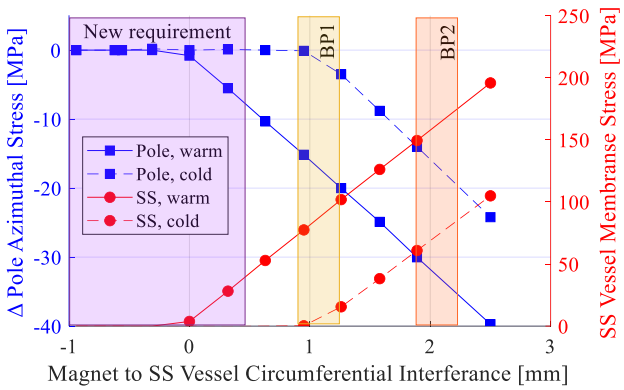

Fig. 6. Coil pre-load increases and stainless-steel vessel membrane (or azimuthal) stress as a function of the magnet to stainless steel vessel circumferential interference at warm. Results obtained using a 2D FE model.

in the coil, was implemented in May 2022 in the third prototype magnet, MQXFBP3. To address Cause 2, and reduce coil peak stress at room temperature, a novel procedure of bladder and key loading was developed based on stretching the structure also via bladders in the cooling hole channels, eliminating the overshoot during loading [13]. The MQXFB02 magnet was loaded in Summer 2022 using the optimized assembly and welding procedure but with already manufactured coils; it will be tested before the end of 2022. Finally, to address Cause 3, improvements on coil fabrication are being explored. MQXFB03 will be assembled with new coils, optimized magnet assembly parameters qualified on MQXFB02, and optimized shell welding parameters qualified on MQXFBP3 and MQXFB02. The production of so-called transition coils has been relaunched to explore various new features and processes; the first transition coil will be assembled with already fabricated coils in a fast-track technical model that is expected to be tested at cold with trim powering scheme in the first half of 2023.

IV. Cold Mass Assembly

A. New Requirements on Shell Welding

Once the loading is completed, the magnet is surrounded by a vacuum tight stainless-steel shell for helium enclosure. The stainless shell (SS) and everything it contains is designated as the "cold mass". In the case of LHC dipole and IR quadrupole magnets ([14],[15]), the stainless shell was designed to complete the mechanical integrity of the cold mass. This was achieved by relying on the weld shrinkage to put the shell into tension and compress the structure inside. In the case of the LMQXFB cold mass, the main function of the SS shell is LHe containment and it is not needed for mechanical support. On the contrary, when the two 8-mm thick stainless-steel half shells of the LMQXFB cold mass are welded together, the weld shrinkage may increase the coil pre-load. This pre-load increase may cause excessive conductor strain if the interference between magnet and cold mass is not limited. In addition, friction may prevent sliding of the aluminum/low-carbon steel magnet structure with respect to the stainless-steel shell during

cool-down and warm-up, resulting in non-uniform, non-reproducible and potentially deleterious axial loads on the brittle conductor. The question then arises on how to avoid or limit the mechanical coupling between outer stainless-steel shell and magnet structure

Figure 6 represents the variation of stainless-steel shell membrane stress (in red, continuous lines) and of the coil pole azimuthal stress (in blue, continuous lines) as a function of the warm circumferential interference, defined as the difference between the inner circumference of the stainless-steel vessel and the outer circumference of the aluminum cylinder after magnet pre-load. The dashed lines represent the situation after cool-down. The cool-down causes a larger shrinkage of the magnet compared to the stainless-steel shell, corresponding to a variation of the interference of 0.9 mm.

In the initial phase of MQXFB development, the target pre-stress in the stainless-steel shell was 75 MPa, to assure that shell is still in contact with the magnet aluminum rings after cool-down. This corresponds to an increase of the coil azimuthal compression of around 8 MPa (8 ± 8 MPa). The first two prototypes were welded using this target, with 15-20 MPa increase of coil pre-stress in MQXFBP1 and 30-35 MPa in MQXFBP2. After the cold powering test of MQXFBP2, the target welding pre-stress was modified to assure no coupling of the stainless-steel shell to the magnet structure, with a target of having in average no increase of the coil azimuthal pre-stress due to welding and a local maximum allowed of 8 MPa.

B. *New Requirement on Fixed Point*

The choice of de-coupling the shell from the magnet structure gave rise to a new issue that was not present for LHC dipole and IR quadrupole magnets: the cryo-magnet must be able to withstand the loads appearing during handling, transport, and operation. The stainless-steel shell itself is well anchored to the magnet cryostat through supporting feet, but if the magnet is loose inside the shell, a fixed point must be introduced between the magnet and the shell. In the case of CERN, it was decided to adopt one single fixed point at the magnet center.

During transport, the maximum acceleration admissible is 0.5 g, consistent with the requirements set for HL-LHC cryo-magnets for any local transport done by CERN. This requirement is set based on the LHC requirement for Short Straight Section (SSS) transport ([16],[17]). The estimated weight of the magnet is 11 tons, so the fixed point shall be designed for a minimum load of 55 kN.

During operation of the cryogenic system, the MQXFB magnet inside its cold mass shall not move when subject to 4 bar (96 kN) differential pressure between the ends of each MQXFB magnet in accordance with a global pressure gradient of 5 bar over the cold mass length (induced by cryogenic operation or by quench of other magnets) and shall withstand this load without physical damage or performance degradation [18]. In summary, the fixed point is designed to hold a horizontal force of 55 kN at room temperature and 96 kN at cryogenic temperature.

To hold this force, the two-tack welding blocks in the middle of the magnet are replaced by a 30 mm diameter pin, in tight contact with the yoke, to have a link between the stainless-steel vessel and the magnet The fixed point is in the middle such that the differential thermal contraction between magnet and stainless-steel shell can be compensated in both sides. For series magnets, the 45 mm-thick central yokes of the magnet will be replaced by a 91.5 mm-thick yoke, such that such that even if the longitudinal stiffness provided by the adjacent thin laminations is neglected, the stand-alone yoke can hold the forces. This solution is implemented from magnet MQXFB02, and it was validated in a mock-up test at room and cryogenic temperatures [19].

C. *Implementation in MQXFBP3*

MQXFBP3 was assembled in the last quarter of 2020 with coils 115, 117, 118 and 119, produced from January to August 2020. The cold mass was welded beginning of 2021, but after the cold powering test of MQXFBP2 the decision was to re-do the cold mass with the welding requirements. The 30 mm hole to host the fixed point was machined in the 45 mm thick central yoke after magnet assembly. In order to verify that the drilling of a hole in the coil vicinity does not impact the magnet performance, the 30 mm hole to host the fixed point was

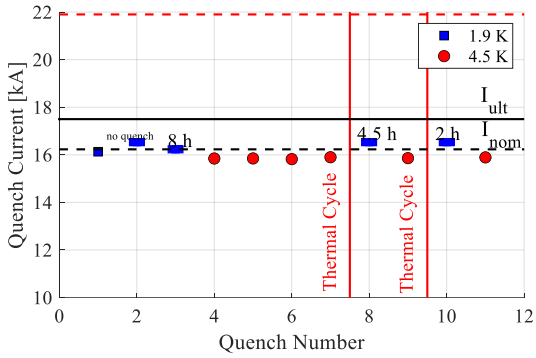

Fig. 7. Training of MQXFBP3. Horizontal line indicates that the current level is reached without quench and the number indicate the length of the current plateau.

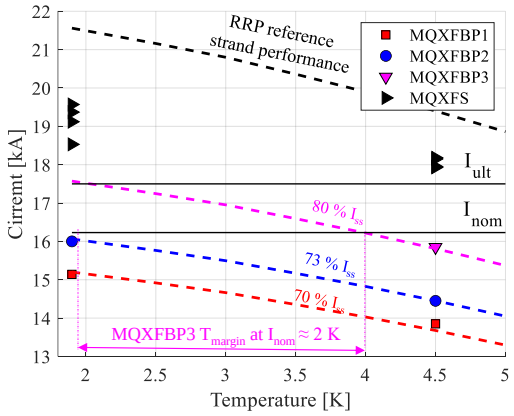

Fig. 8. Performance limit of MQXF magnets. Maximum reached current as a function of the bath temperature for MQXFBP and MQXFS magnets (MQXFS4, S5, S7 and S7). Horizontal lines represent the nominal and ultimate currents for operation in the LHC. Dotted lines show the expected performance of the conductor at different levels of the short sample limit.

machined in MQXFS7d. Power test at 1.9 K demonstrated no performance degradation up to current levels well above operational values. To avoid interference between stainless-steel vessel and magnet after welding, a gap between the top shell and the magnet structure was set to compensate the welding shrinkage. The measured membrane stress in the shell at the end of the welding was close to zero in the upper shell, 30 MPa in the bottom shell. The increase of coil compression during the welding was less than 1 MPa, fulfilling the new requirements.

MQXFBP3 was tested in September 2022, reaching the target current of 16.53 kA (I_{nom} + 300 A) at 1.9 K after one training quench (see Fig. 7). At 4.5 K, the maximum current was 15.85 kA showing a performance limitation with a similar phenomenology to the one observed in the previous two prototype magnets. The extrapolation to 1.9 K of the quench level achieved at 4.5 K (see Fig. 8) provides an estimated quench level limitation around ultimate current of 17.54 kA and 2 K temperature margin for operation at nominal current and 1.9 K. In operation, debris from proton-proton collisions at the interaction's points induce energy deposition in the superconducting magnets. For MQXF, the maximum expected temperature increase due to debris-generated energy deposition for baseline luminosity and collision energy is 0.32 K [20], so MQXFBP3 temperature margin is 6 times larger than the expected temperature rise in the conductor during operation.

The magnet showed good memory after warm-up/cooldown to room temperature with no retraining at 1.9 K and the performance at 4.5 K was not affected by temperature and current cycles. Field errors are below 1 unit and the stability of the field was measured during the 8 hours plateau at nominal current, showing no change on the gradient within the 1 unit measuring precision.

V. Magnet Assembly

A. Design and requirements

Assembly of MQXF magnets relies on a system of water-pressurized bladders and keys to pre-compress the coils and to pre-tension the aluminum cylinder during loading at room temperature (RT) [21]. The coil pre-load increases after cool-down to 1.9 K thanks to the larger thermal contraction of the aluminum shrinking cylinder with respect to the rest of the magnet components. The target pre-load levels for Al-shells, coils and rods are chosen based on the experience of short models [6], [22]. The goal is to achieve after cool-down an azimuthal pre-compression of 100-110 MPa in the Ti coil pole, which corresponds to a RT target average azimuthal stress on coils and aluminium shrinking cylinders −80 ±8 MPa and +58 ±6 MPa respectively [23]. By inflating the bladders at progressively higher pressures, a clearance is opened to enable key insertion; the key size is progressively increased to obtain the target preload on the Al-shells and coils. Experimental results on short models and long magnets have shown that the bladder inflation step leads to a coil stress overshoot with respect to the final assembled state.

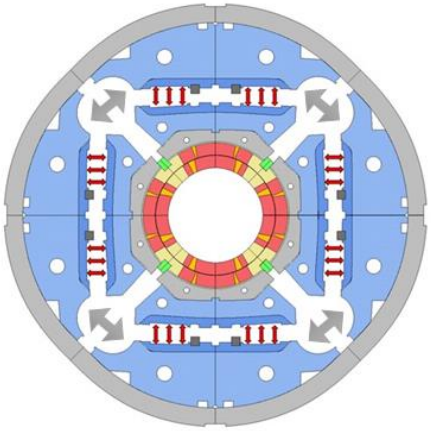

Fig. 9. MQXF magnet cross section indicating the position of the bladders. Red arrows correspond to the standard bladder location. Grey arrows show the additional bladders in the heat exchanger holes added in MQXFB02.

As well known in the literature, this overstress may be critical for Nb_3Sn (see for example [24]). Recent studies have shown that Nb_3Sn filament micro-cracking can be induced at transverse stress level below the threshold of critical current degradation [25].

For this reason, significant work is ongoing on MQXF cable stacks to determine the relationship between transverse compressive stresses and radial crack initiation and propagation reproducing magnet operational conditions. The first results indicate that the level of azimuthal compression for micro-crack initiation is 110-120 MPa [25]. In the MQXF short model program, the measured peak compression in the coil was 140 MPa for magnets reaching more than 90 % of the short sample limits, well above the performance requirements for operation in the LHC (see Fig. 8). At the early stage of the MQXFB program, a value of 150 MPa was chosen as the upper bound for azimuthal compression during loading [26]. A more conservative approach was subsequently chosen by AUP, setting 120 MPa as the maximum compression level that shall never be exceeded [23][26]. High pre-load studies in TQS03 magnet showed no performance degradation up to 220 MPa at cold, and 5 % degradation for 260 MPa peak stress at cold which corresponds to a 125 MPa pole stress after loading [27]. Similar studies are on-going in MQXF short model magnet program.

To reduce the overshoot on the coil stress during loading, a new bladder procedure was developed for MQXFB magnets [13], introducing auxiliary bladders in the heat exchanger holes (see Fig. 9). The additional bladders allow the stretching the aluminium shell without increasing the coil compression, drastically reducing coil azimuthal stress during loading operations. With the new loading procedure, the maximum coil pole compression level that shall never be exceeded in MQXFB magnet assembly is 100 MPa, with a RT target average azimuthal stress on coils and aluminium shrinking cylinders of -70 ±10 MPa and +58 ±6 MPa. With the new proce-

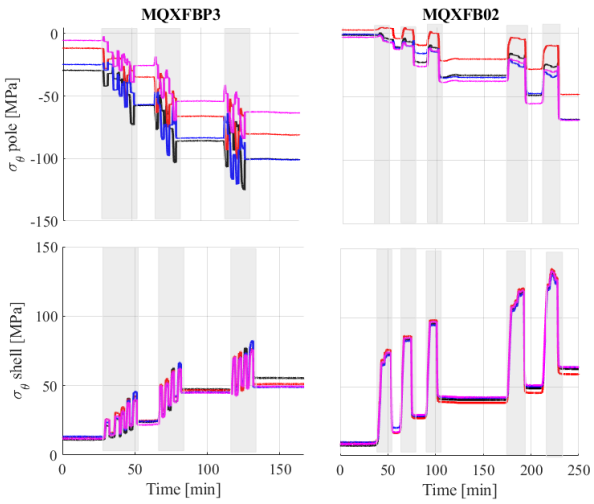

Fig. 10. Coil pole (top) and Al-shell (bottom) azimuthal stress during assembly. The left plots correspond to MQXFBP3 and the right plots to MQXFB02. Grey rectangles indicate the bladder operations.

dure, the target RT coil pre-stress is 10 MPa lower for the same pole compression after cooling down due to frictional effects in the structure [13].

B. Implementation in MQXFB02

The coils assembled in MQXFB02 (121, 123, 124 and 125) were manufactured from October 2020 to April 2021. The magnet was loaded in July 2022 using the new procedure after validating the methodology in a full-length mechanical assembly test (MQXFBMT3) and in a short model magnet (MQXFS7e) [13]. The difference in coil pole azimuthal stress (top) and Al shrinking cylinder azimuthal stress (bottom) for the previous procedure and the new procedure with auxiliary bladders can be seen in Fig. 10, where the measurements during MQXBP3 and MQXFB02 loading in the middle of the magnet are plotted: during bladder operations, the stress in the coil pole with the new procedure is lower than the final coil pole azimuthal stress once the keys are inserted. On the other hand, the stress in the Al-shell during loading is higher with the new procedure, but it is still well and safely below the yield limit of the material (420 MPa at room temperature). Comparing the results of MQXFBP3 and MQXFB02, the maximum pole azimuthal stress during loading decreases from 120 MPa to less than 40 MPa whereas the stress in the Al-shell increases from 80 MPa to 140 MPa.

VI. Coil Fabrication

A. Introduction

The production of MQXFB coils started in 2016, with the completion of the coils for the MQXFBP1 after summer 2018 [28]. Following a series of critical nonconformities, coil fabrication was on hold for about six months in 2019 to review manufacturing procedures, improve the robustness of the process and set up of a core and stable production team. In September 2019 coil fabrication resumed, with a production flow of approximately one coil per month [29]. In April 2021, after the cold powering test of MQXFBP2, coil production was on hold to identify potential issues during coil manufacturing and/or handling leading to the performance limitation of the first two prototype magnets. The coils of MQXFB02 were already completed before the stop of the coil production. Beginning of 2022, the results from coil post-mortem inspection identified a very localized defect in the pole-to-pole transitions, focusing the analysis on that specific location (see section II).

B. Findings

a) Coil 'hump' after reaction

The cable is wound around a segmented Ti pole keeping a tension on the cable of 19 kg in the straight section and 7 kg in the ends. Gaps are placed between pole segments to allow the coil to contract in the longitudinal direction from the winding tension and from the expected conductor contraction during heat treatment [30]. The goal is to have the gaps closed after reaction. The initial assumed length of contraction was 17.6 mm (2.5 mm/m) distributed over 16 gaps. After the production of 5 coils, the integrated initial pole gap was reduced to 14.4 mm. After releasing the winding tension, the gap between poles decreases mostly in the coil ends. The coil then is placed in a reaction mold and heat treated in an oven under argon flow to form Nb_3Sn. The reaction process requires three plateaus at 210 ºC, 400 ºC and 665 ºC. After reaction, poles gaps are almost closed [29]. A vertical deviation of the pole tip with respect to the base plate was observed from coil 111, wound in October 2019 (this measurement was not carried out on previous coils). This so-called *coil hump* was systematically observed in Nb_3Sn coils produced by standard procedures but was not present in coils wound with copper conductor. For Nb_3Sn coils, the maximum amplitude is $\approx$ 2 mm in the longitudinal center of the coil. Figure 11 shows the measured average and standard deviation coil hump in all RRP coils made after coil 111 using standard procedures.

b) Coil 'belly' after impregnation

The coil is then closed in the impregnation mold and CTD-101 K® resin is injected at 60 ºC inside a vacuum tank. The typical injection time is three hours. The epoxy curing is done at 2 bars pressure in two plateaus, the first at 110 °C for 5 h and the second at 125 °C for 16 h. After impregnation, each coil is measured in 43 longitudinal cross sections, using the coil outer diameter and pole keyway as alignment for the best fit to reproduce the functional magnet configuration [31]. MQXFB coils show a systematic larger azimuthal size in the middle of the coils, with typically 0.150 mm larger azimuthal excess (left + right mid-plane) in the middle of the coil. The so-called *coil belly* was observed in Nb_3Sn coils produced with standard procedures and not present in copper coils, and it is summarized in Fig 12. Comparing Figures 11 and 12, it

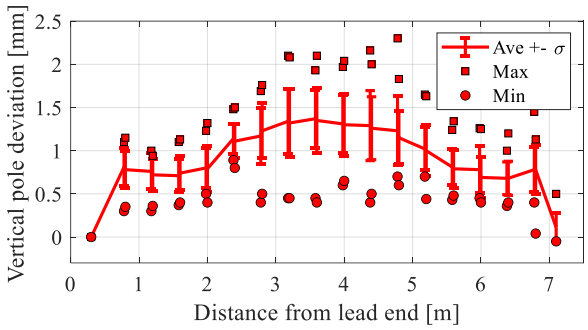

Fig 11. Vertical deflection of the pole with respect the base plates measured (the so-called coil hump). The data contains the average, standard deviation, maximum a minimum deviation of the last 15 Nb_3Sn coils.

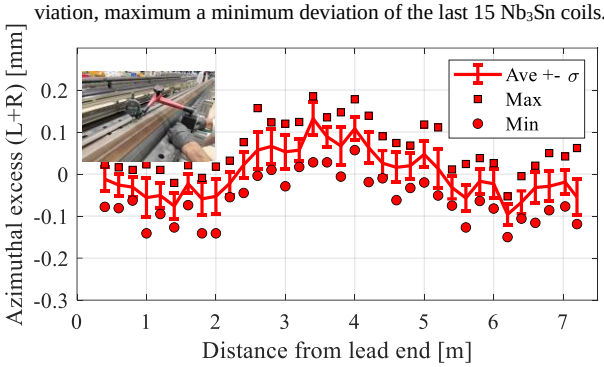

Fig 12. Variation along the length of the azimuthal coil excess after impregnation (the so-called coil belly). The data contains the average, standard deviation, maximum a minimum deviation of the last 15 Nb_3Sn coils

should be note that the hump and the belly seem to be correlated. This feature is not present in MQXFA coils produced at Fermilab or BNL.

c) Possible mechanism of performance limitation

MQXFB coils are the longest Nb_3Sn coils for accelerator magnets ever manufactured. The cavity of the reaction fixture was designed assuming an expansion of the conductor of 4.5 % in the azimuthal direction and 1.2 % in the radial direction. Experiments on strands, cables, and coils (insulated/non-insulated) have shown that the volumetric expansion of the conductor is ≈ 3 %, but the azimuthal, radial and axial expansion depends on the way the cable is constrained [32]. A possible mechanism for the occurrence of the *hump*, and, subsequently, of the *belly*, is that, due to the friction between coil and tooling, and in spite of the large room for expansion of the conductor during heat treatment assumed in the design, the coil is not free to slide uniformly in the fixture, and, at the end of the end treatment cycle, remains partially constrained with some stored energy. When the reaction fixture is open and the coil is in free state, the stored energy is released, resulting in the vertical displacement of the coil pole and pole turn by 1-2 mm in the coil center (coil *hump*). Transverse bending resulting on sub-element breakage might happen during the opening of the fixture or when the *hump* is put back in place during the closure of the impregnation fixture.

In preparation for impregnation, the coil is rotated 180 degrees, and, when supported on the outer diameter, a 2 mm excess per mid-plane is measured near the coil center, consistent with the observed coil hump when the coil is sitting on the inner radius and mid-planes. During impregnation, the coil is rigid enough to deform the impregnation tooling resulting in the 0.15 mm larger excess in the middle (coil *belly*).

d) Additional Observations on Coil 126

A set of additional measurements were performed in coil 126. This coil was on hold after curing in April 2021 and reacted in February 2022. The reaction and impregnation fixtures were closed monitoring the required torque on the set screws. The measurements show that whereas a uniform torque is needed to close the reaction fixture, the torque needed to close the middle of the impregnation fixture is about two times the torque needed to close the coil closer to the ends, consistent with the presence of the *hump*.

In addition, on coil 126, pressure sensitive film was placed on the outer and inner diameter of the coil during the impregnation mold closure. The imprint of the outer layer was uniform, but the inner layer showed local stress concentrations at the Ti pole transitions (see Fig. 13). After impregnation, the coil was cut to perform metallurgical inspection. Two out of the 8 transitions examined showed broken sub-elements, demonstrating that the damage can be present in a coil before assembly and test. In coil 126, not only the strand at the upper edge of the inner layer pole turn was affected but also strands at the upper edge of the outer layer pole and mid-plane turns. Nevertheless, the extension of the damage in the longitudinal cut was only 3 mm over a 50 mm length segment. Coil 126 was closed two times in the impregnation fixture which could have had a detrimental effect on the presence of broken filaments.

e) Transition coils

With this mechanism in mind, the production of transition coils is ongoing with the aim of reducing the coil stored energy after heat treatment.

The first transition coil, 127, is mainly addressing the longitudinal behavior, increasing the pole gaps to provide more space to the coil during reaction. Nevertheless, the macroscopic observables of the coil after heat treatment were similar to previous coils. The plan is to test coil 127 with the non-limiting coils of MQXFBP1 to assess its performance.

The goal of the second transition coil, 128, is to reduce the radial friction during heat treatment. The outer layer is cured without ceramic binder and a 1 mm shim per mid-plane is added in both layers during curing, to reduce the size of the coil before reaction. The heat treatment of the coil is currently ongoing. The coil is presently undergoing heat treatment.

New generation coils will also implement other features such as the addition of a 0.05 mm thick layer of E-glass be-

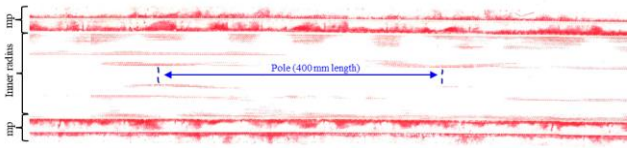

Fig. 13. Pressure sensitive film imprint (2.5-10 MPa) of the inner radius and mid-planes after the closure of the impregnation fixture. The blue line indicates the length of the titanium pole.

tween the quench heater polyimide and the insulated conductor to increase the heater to coil dielectric strength [33]. The copper plated stainless steel heater strips are now encapsulated in between two layers of polyimide to improve the mechanical robustness of the component and the qualification tests before installation in the coil are performed at a voltage level of 8 kV instead of 3.7 kV.

VII. Conclusions

The power tests of the two first quadrupole magnet prototypes MQXFBP1 and MQXFBP2 have validated many features of the design such as field quality and quench protection but have found a performance limitation below nominal current with a very similar phenomenology. Metallographic inspections of the limiting coil of MQXFBP1 revealed the presence of damaged strands in the area of quench start localization, with longitudinally broken Nb_3Sn sub-elements, pointing to a thermomechanical origin for the performance limitation.

Following the results of MQXFBP1 and MQXFBP2, a thorough root cause analysis was carried out and a 3-stage program was initiated to address the possible root causes.

The first stage addresses the mechanical coupling between the outer stainless-steel shell and the magnet structure, which was reduced to a minimal in the assembly of the third quadrupole magnet prototype (relying on an already existing magnet assembly with already manufactured coils). MQXFBP3 showed a performance improvement with respect to MQXFBP1&2 and was able to achieve nominal current + 300 A at 1.9 K. However, it still shows a limitation at 4.5 K, slightly below nominal current, with a phenomenology similar to the one observed on MQXFBP1&2.

The second stage addresses coil overstress during magnet loading, which has been resolved and eliminated using additional bladders implemented in the yoke cooling holes. The new procedure was successfully applied to the loading of MQXFB02 (relying on already manufactured coils). The cold mass assembly of MQXFB02 was completed using the new stainless-steel shell welding procedure validated on MQXFBP3 and will be cold tested before end of 2022.

The third stage addresses issues related to coil manufacturing and handling, which are being dealt with in a systematic manner through the manufacturing and, eventually, cold testing of transition coils.

The spectacular progress in postmortem coil inspections through tomography and microstructural investigations have enabled a clear identification of the limitation origins and are proving essential in the development of corrective/mitigation actions.

Acknowledgments

The authors wish to thank the CERN TE-MSC technical staff for the construction and cold powering tests of the magnets and for the strong and continuous support of the CERN TE and HL-LHC project managements.

References

[1] O. Bruning et al, “LHC design report” Vol. 1, CERN 2004-003.
[2] E Todesco *et al* 2021 *Supercond. Sci. Technol.* 34 053001
[3] P. Ferracin et al., “Magnet design of the 150 mm aperture low-β quadrupoles for the high luminosity LHC,” *IEEE Trans. Appl. Supercond*., vol. 24, no. 3, Jun. 2014, Art. no. 4002306.
[4] G. Ambrosio, et al., “Lessons learned from the prototypes of the MQXFA Low Beta Quadrupoles for HL-LHC and plans for production in the US,” *IEEE Trans. Appl. Supercond.*, submitted for publication.
[5] S. A. Gourlay et al., “Magnet R&D for the US LHC accelerator research program,” *IEEE Trans. Appl. Supercond.*, vol. 16, no. 2, pp. 324–327, Jun. 2006.
[6] P. Ferracin, et al., “The HL-LHC Low-β Quadrupole Magnet MQXF: From Short Models to Long Prototypes,” *IEEE Trans. Appl. Supercond.*, vol. 29, no. 5, Aug. 2019, Art. no. 4001309.
[7] E Takala *et al* 2021 *Supercond. Sci. Technol.* 34 095002
[8] R. Keijzer et al, “Effect of Strand Damage in Rutherford Cables on the Quench Propagation in Nb_3Sn Accelerator Magnets,” *IEEE Trans. Appl. Supercond.*,’ submitted for publication
[9] F. J. Mangiarotti et al., "Power Test of the First Two HL-LHC Insertion Quadrupole Magnets Built at CERN," in *IEEE Transactions on Applied Superconductivity*, vol. 32, no. 6, pp. 1-5, Sept. 2022, Art no. 4003305, doi: 10.1109/TASC.2022.3157574.
[10] E. Ravaioli, “CLIQ,” Ph.D. dissertation, Univ. Twente, 2015
[11] A. Moros et al., "A metallurgical inspection method to assess the damage in performance-limiting Nb_3Sn accelerator magnet coils", submitted for publication
[12] I. Aviles Santillana, S. Sgobba et al., "A metallurgical inspection method to assess the damage in performance-limiting Nb_3Sn accelerator magnet coils", submitted for publication
[13] J. Ferradas Troitino et al., "Optimizing the use of pressurized bladders of the assembly of superconducting magnets: the HL-LHC MQXFB quadrupole magnet case," submitted for publication
[14] N. Andreev et al., "Mechanical design and analysis of LHC inner triplet quadrupole magnets at Fermilab," in *IEEE Transactions on Applied Superconductivity*, vol. 10, no. 1, pp. 115-118, March 2000, doi: 10.1109/77.828189.
[15] A. Yamamoto et al., "Production and measurement of the MQXA series of LHC low-/spl beta/ insertion quadrupoles," in *IEEE Transactions on Applied Superconductivity*, vol. 15, no. 2, pp. 1084-1089, June 2005, doi: 10.1109/TASC.2005.849501.
[16] K. Artoos et al., Mechanical dynamic analysis of the lhc arc cryo-magnets, Proceedings of the 2003 Particle Accelerator Conference https://accelconf.web.cern.ch/p03/PAPERS/TPAG007.pdf
[17] K. Artoos et al., Mechanical dynamic load of the lhc arc cryomagnets during the installation cern-ts-2004-010 (ic), EDMS Nr. 480679. https://cds.cern.ch/record/1068845/files/ts-2004-012.pdf
[18] R. Van Weelderen, private communication, 2022
[19] O. Sacristan de Frutos et al., ‘Mechanical testing of the new fix point for MQXFB stainless stell shell’, CERN internal report, EDMS 2711705
[20] P. Borges de Sousa, et al., “Numerical Assessment of the Inhomogeneous Temperature Field and the Quality of Heat Extraction of Nb_3Sn Impregnated Magnets for the High Luminosity Upgrade of the LHC,” *IEEE Trans. Appl. Supercond.*, submitted for publication.
[21] S. Caspi, et al., “The use of pressurized bladder for stress control of superconducting magnets,” *IEEE Trans. Appl. Supercond.* 11 (2001) 2272-2275
[22] S. I. Bermudez et al., "Performance of a MQXF Nb_3Sn Quadrupole Magnet Under Different Stress Level," *in IEEE Transactions on Applied Superconductivity*, vol. 32, no. 6, pp. 1-6, Sept. 2022, Art no. 4007106, doi: 10.1109/TASC.2022.3167369.
[23] P. Ferracin et al., "Assembly and Pre-Loading Specifications for the Series Production of the Nb3Sn MQXFA Quadrupole Magnets for the HL-LHC," in *IEEE Transactions on Applied Superconductivity*, vol. 32, no. 6, pp. 1-6, Sept. 2022, Art no. 4000306, doi: 10.1109/TASC.2022.3148971.
[24] J. W. Ekin, “Effect of transverse compressive stress on the critical current and upper critical field of Nb_3Sn,” J. Appl. Phys., vol. 62, no. 12, pp. 4829–4834, 1987.

[25] K. Puthran et al., "Onset of mechanical degradation due to transverse compressive stress in Nb3Sn Rutherford type cables", submitted for publication

[26] Patrick Ebermann *et al* 2018 *Supercond. Sci. Technol.* 31 065009

[27] H. Felice et al., "Performance of a Nb_3Sn Quadrupole Under High Stress," in *IEEE Transactions on Applied Superconductivity*, vol. 21, no. 3, pp. 1849-1853, June 2011, doi: 10.1109/TASC.2010.2090116.

[28] Lackner *et al.*, "Status of the Long MQXFB Nb_3Sn coil prototype production for the HiLumi LHC," *IEEE Trans. Appl. Supercond.*, vol. 27, no. 4, Jun. 2017, Art. no. 4002605.

[29] S. I. Bermudez et al., "Progress in the Development of the Nb3Sn MQXFB Quadrupole for the HiLumi Upgrade of the LHC," in *IEEE Transactions on Applied Superconductivity*, vol. 31, no. 5, pp. 1-7, Aug. 2021, Art no. 4002007, doi: 10.1109/TASC.2021.3061352.

[30] C. Scheuerlein et al., "Phase transformations during the reaction heat treatment of N_b3Sn," in Journal of Physics: Conference Series. 2010. 234. 10.1088/1742-6596/234/2/022032.

[31] J. Ferradas Troitino et al., "Applied Metrology in the Production of Superconducting Model Magnets for Particle Accelerators," in *IEEE Transactions on Applied Superconductivity*, vol. 28, no. 3, pp. 1-6, April 2018, Art no. 4002106, doi: 10.1109/TASC.2017.2786262.

[32] E. Rochepault et al., "Dimensional Changes of Nb3Sn Rutherford Cables During Heat Treatment," in *IEEE Transactions on Applied Superconductivity*, vol. 26, no. 4, pp. 1-5, June 2016, Art no. 4802605, doi: 10.1109/TASC.2016.2539156.

[33] V. Marinozzi et al., "Study of the Heater-Coil Electrical Insulation for the HL-LHC Low Beta Quadrupoles," in *IEEE Transactions on Applied Superconductivity*, vol. 31, no. 5, pp. 1-5, Aug. 2021, Art no. 4001705, doi: 10.1109/TASC.2021.3061348.